Accepted Manuscript

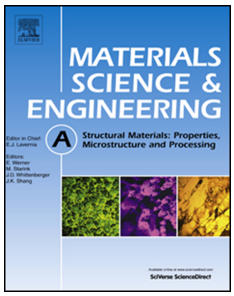

Superior mechanical properties and deformation mechanisms of heterogeneous laminates under dynamic shear loading

Jinyan He, Fuping Yuan, Muxin Yang, Sihai Jiao, Xiaolei Wu

PII: S0921-5093(19)30555-6

DOI: https://doi.org/10.1016/j.msea.2019.04.082

Reference: MSA 37832

To appear in: *Materials Science & Engineering A*

Received Date: 22 January 2019

Revised Date: 18 April 2019

Accepted Date: 20 April 2019

Please cite this article as: J. He, F. Yuan, M. Yang, S. Jiao, X. Wu, Superior mechanical properties and deformation mechanisms of heterogeneous laminates under dynamic shear loading, *Materials Science & Engineering A* (2019), doi: https://doi.org/10.1016/j.msea.2019.04.082.

Superior mechanical properties and deformation mechanisms of heterogeneous laminates under dynamic shear loading

Jinyan He[a,b], Fuping Yuan[a,b*], Muxin Yang[a], Sihai Jiao[c], and Xiaolei Wu[a,b]

hejinyan@imech.ac.cn, fpyuan@lnm.imech.ac.cn, mxyang@lnm.imech.ac.cn,

shjiao@baosteel.com, xlwu@imech.ac.cn

[a]State Key Laboratory of Nonlinear Mechanics,

Institute of Mechanics, Chinese Academy of Science,

15 Beisihuan West Road, Beijing 100190, China

[b]School of Engineering Science, University of Chinese Academy of Sciences,

19A Yuquan road, Beijing 100049, China

[c]Baosteel Research Institute, Baoshan Iron & Steel Co., Ltd., Shanghai 201900, China

Corresponding author: fpyuan@lnm.imech.ac.cn (F.P. Yuan) Tel.: 86-10-82544409,

Fax: 86-10-82543977

Abstract

High-strain rate response of low C steel/304 stainless steel (SS) laminates was characterized by hat-shaped specimen using Hopkinson-bar technique at a strain rate of about 7×10^4 s^{-1}. Better dynamic shear properties were observed in the laminates, compared to the plain low C steel plate and the plain 304 SS plate. The laminates were found to postpone the nucleation of adiabatic shear band (ASB) in the hard zone and to delay the propagation of ASB from the hard zone to the soft zone. The conventional maximum stress criterion on ASB nucleation was found not valid any more in the laminates. The hardness difference between the hard zone and the soft zone in the laminates was found to have great influence on the patterns of ASB evolution. Nanotwins were formed in the 304 SS and grain refinement was observed in the martensite low C steel for strain hardening under dynamic shear loading. The mechanical incompatibility across the interfaces was observed to result in strain gradient and geometrically necessary dislocations at the interfaces under dynamic shear loading, contributing to extra strain hardening. The extra hardening was also found to be triggered at the propagation tip of ASB, which helps for achieving better dynamic ductility in the laminates.

Key words: Laminates; Twinning; strain gradient; geometrically necessary dislocations; Dynamic fracture; Shear band.

1. Introduction

Superior combination of strength and ductility in metals and alloys has been pursued by scientists and engineers for several decades [1-8]. While these two properties are mutually exclusive in general, i.e., high yield strength usually results in limited ductility. In the last two decades, several heterogeneous microstructures have been proposed to produce both high yield strength and large tensile ductility in metals and alloys, such as bimodal/multimodal structures [1,9], gradient structures [10-13], lamella structures [8,14,15], and bimetallic laminates [16-26]. These heterogeneous microstructures generally have various domains with different mechanical properties, and the plastic deformation incompatibility can occur among these domains [8,27-29]. Thus, stress/strain partitioning and back stress hardening have been reported to play important roles in the plastic deformation of these heterogeneous microstructures [8,17,27-29]. Among these heterogeneous microstructures, bimetallic laminates have great advantages for structural applications due to the fact that superior tensile properties can be achieved by regulating microstructural parameters, such as microstructures across the interface, hardness difference between plates, and interface spacing [16-26].

The mechanical properties and the deformation mechanisms in bimetallic laminates have been widely studied and well understood under quasi-static conditions [16-26], while their plastic deformation behaviors under high strain rates are still unclear until now. As we know, the flow and facture behavior of materials under impact loading should be dramatically different from that under quasi-static conditions since thermal softening induced by adiabatic heating, strain rate effect and inertia effect can significantly affect the plastic deformation and fracture mechanisms [30-35]. The mechanical behaviors under high strain rates in metals and alloys with homogeneous

microstructures have been investigated extensively [36-43]. Typically, the metals and alloys with high dynamic yield strength have low critical strain for onset of adiabatic shear band (ASB) and low impact toughness, in other words, there still exits a strength-toughness contradiction under dynamic loading for metal and alloys with homogeneous microstructures. In previous work [44-46], heterogeneous microstructures, such as heterogeneous grain structure and gradient structure, have been reported to have superior dynamic strength-toughness combination under dynamic shear loading that is not accessible to homogeneous materials.

In heterogeneous grain structure and gradient structure, the dynamic shear properties can be significantly improved by the stress/strain partitioning among different domains with various grain sizes and the back stress hardening [44-46], while no obvious interfaces exist in these heterogeneous microstructures. The interfaces have been reported to significantly strengthen and toughen bimetallic laminates under quasi-static conditions, the strain gradient and the pile-up of geometrically necessary dislocations (GNDs) near the interface zone have been found to play important roles in the strengthening and toughening [16,17,25,26]. While, how the interfaces affect the dynamic shear properties and the evolution of ASB in bimetallic laminates is still in vague. Moreover, the hardness difference between the hard zone and the soft zone in the laminates might have great impact on the evolution pattern of ASB, and this effect is needed to be symmetrically investigated. In this regard, low C steel/304 stainless steel (SS) laminates by hot-rolled (HR) bonding (commercially produced in Baosteel, China) were used in this work as a studying case to investigate the dynamic shear response using the hat-shaped specimens in Hopkins bar. The microstructures can be "frozen" at some specified dynamic strain using controlled height of the stop ring during the dynamic shear testing. The microstructure observations at the interrupted shear

displacements were also conducted for the "frozen" specimens to study the dynamic shear deformation mechanisms.

2. Materials and experimental methods

The low C steel has the chemical composition of 0.2C-1.0Mn-0.02Ti-0.04Nb, while the chemical composition for the 304 SS is 0.05C-1.2Mn-19Cr-10Ni (all in mass % and with the balance of Fe). The laminates are composed of two 304 SS plates at the two sides and one low C steel plate in the center. The plates were combined into the laminates by hot rolling (HR) between 1423 K and 1173 K. The resultant HR laminates have a thickness of 3.3 mm, and the thickness ratio is 1:8:1 (304 SS to low C steel to 304 SS). Three different samples with different heat treatment conditions were used in the present study: the first one is the sample manufactured by HR (identified as HR sample), the second one is the sample annealed at 1073 K for one hour after HR (identified as AN sample), and the third one is the sample annealed at 1193 K for 15 min followed immediately by water quenching (identified as WQ sample).

The set-up of hat-shaped experiments in Hopkinson bar, the geometry and dimensions of the hat-shaped specimens and the specimen holders are displayed in Fig. 1. The design of hat-shaped specimens have advantages to reveal the ASB evolution in metals and alloys [30,38,40], compared to other methods for dynamic shear loading [32,42]. Due to the nature of laminates, flatted specimens were used in the present study for dynamic shear testing, thus cylindrical maraging steel holders with ultra-high strength were also used to ensure a nearly pure shear deformation by constraining the lateral expansion of two legs and control the specific shear displacement to "frozen" the microstructure by changing the height of the holders. The other details for the dynamic

shear testing can be referred to [43-45]. Based on the one-dimensional elastic stress wave theory, the shear stress and the shear displacement in the specimens under dynamic shear loading can be calculated as follows:

$$\tau_s = E(\frac{A}{A_s})\varepsilon_T \tag{1}$$

$$U_s = 2C_0\int_0^t \varepsilon_R d\tau \tag{2}$$

Where ε_T and ε_R are the transmitted and reflected strain signals measured on the input and output bars by strain gauges, respectively; C_0, E and A are the longitudinal elastic wave velocity, Young's modulus and the cross-sectional area of the input/output bars, respectively; A_s is the area of the concentrated shear zone in the specimens.

In order to compare the dynamic shear properties of laminates with those for their homogeneous constituent plates (i.e., the plain low C steel plate and the plain 304 SS plate), the homogeneous low C steel plates (2.35 mm thick) are obtained by polishing away the two 304 SS thin layers from the laminates. While the homogeneous plain 304 SS plates (2.40 mm thick) are manufactured by annealing at 1193 K for 15 min followed immediately by WQ for a HR 304 SS plate with the same chemical composition. Three tests were conducted for each sample to check the repeatability. Schematics of sample extraction for microstructural examination was also displayed in Fig. 1, i.e., cross-section with shear zones for all three layers was observed. Micro-hardness distributions across the shear zone on the polished sample surfaces before and

after dynamic shear testing were obtained using a Vickers diamond indenter at a load of 5 g for 15 s dwell time. For each position, ten groups of tests were taken and error bars for the micro-hardness were also calculated and provided.

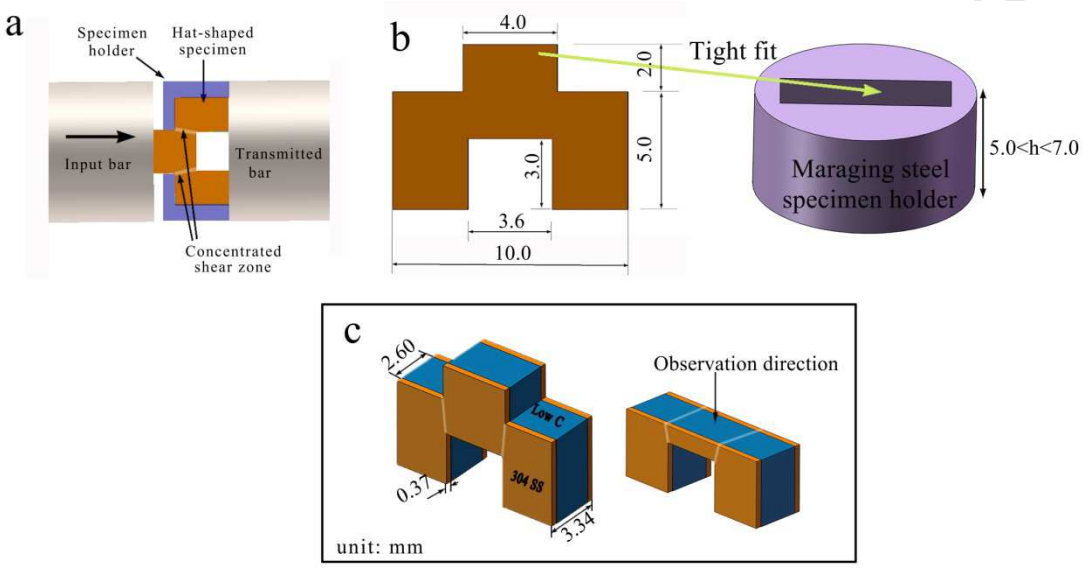

Fig. 1 (a) The set-up of Hopkinson bar experiments with hat-shaped specimens; (b) Schematics of hat-shaped samples for the laminates; (c) Illustration of sample extraction for microstructural examination.

Before and after dynamic shear testing, the microstructures have been characterized by Optical Microscope (OM), Scanning electron microscope (SEM) with back-scattered electron (BSE) mode, electron backscattered diffraction (EBSD) and transmission electron microscope (TEM). The sample preparations for OM, SEM, and EBSD observations can be referred to [26]. In EBSD observation, the scanning step was set to be 100 nm. The first nearest neighbor was used to calculate Kernel average misorientation (KAM), without considering the misorientation larger than 3 degrees [17,47]. For TEM observations, thin disks were first mechanically polished down to

about 20 μm, then the specific location (near the interface) is finally thinned by ion milling or focused ion beam.

3. Results and discussions

3.1 Initial microstructures

Fig. 2 displays the microstructures (EBSD images) of the area near the interfaces for varying samples (HR, AN, WQ samples). The inverse pole figures (IPF) of varying samples are shown in Figs. 2a-2c. The interfaces can be clearly identified as straight lines for varying samples, and the highly heterogeneous microstructures across the interfaces can be observed. For the side of 304 SS, the microstructure and the grain size are similar for varying samples, which is also verified by the hardness distributions near the interface for varying samples later (The hardness for the side of 304 SS is nearly identical for all samples). There exists a gradient distribution of grain size near the interface for the side of 304 SS, and the grain size is smaller at the interface for all samples. The side of 304 SS shows a phase of austenite, and the average grain size in Fig. 2 is about 19, 22, 22 μm for the HR, AN and WQ samples, respectively. Lath martensite are formed during WR on the side of low C steel for the WQ sample, while the low C steel has a phase of ferrite for the HR and AN samples. The inset of Fig. 2c displays a quality chart with a higher magnification for the low C steel in the WQ sample, lath martensite can be clearly observed. The grain size for the side of low C steel is relatively uniform for the HR sample (with an average grain size of 15 μm), while the AR sample has an inhomogeneous microstructure for the side of low C steel (the area close to the interface has a larger average grain size of 75 μm, while the area away from the interface has a smaller average grain size of 11 μm). The microstructure

for the homogeneous plain 304 SS plate is shown Fig. 2d, it is observed that the microstructures (grain size and misorientation distribution) are very similar to those in varying laminates (as shown in Figs. 2e and 2f). This indicates that the made plain 304 SS plate can be considered as the homogeneous constituent plate for varying laminates.

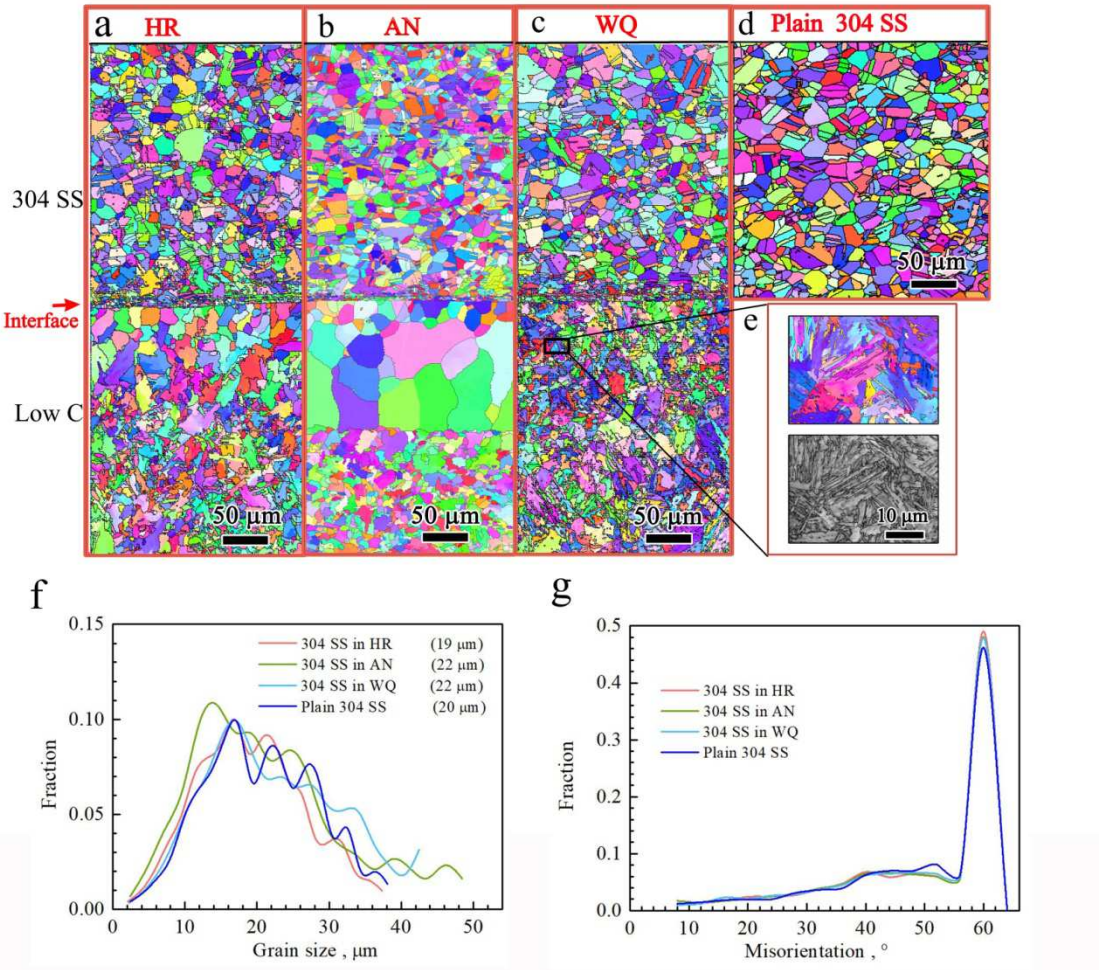

Fig. 2 IPF images near the interface for varying samples: (a) HR sample; (b) AN sample; (c) WQ sample. (d) The IPF image for the prepared plain 304 SS sample. (e) The IPF image and the quality chart with a higher magnification at the side of low C steel for the WQ sample. The lath martensite can be clearly observed. (f) The grain size distributions for the 304 SS in the HR sample, the AN sample, the WQ sample and the

plain sample. (g) The misorientation angle distributions for the 304 SS in the HR sample, the AN sample, the WQ sample and the plain sample.

TEM image for the 304 SS in the WQ sample is shown in Fig. 3a, while Fig. 3b displays TEM image for the martensite low C steel in the WQ sample. The TEM image for the 304 SS was taken nearly at the interface, while the TEM images for the low C steel were taken at a distance of about 100 μm away to the interface. Most grains are equi-axed in the austenite phase of 304 SS, while lath martensite can be easily identified for the martensite phase of low C steel in the WQ sample. For the locations where the numerical TEM images were taken, the statistical distributions for the grain size of the 304 SS austenite phase and the width of the lath martensite phase are displayed in Fig. 3c. Then the average grain sizes or feature sizes at the corresponding locations can be estimated to be about 323 nm for the 304 SS austenite phase and 249 nm for the lath martensite phase, respectively.

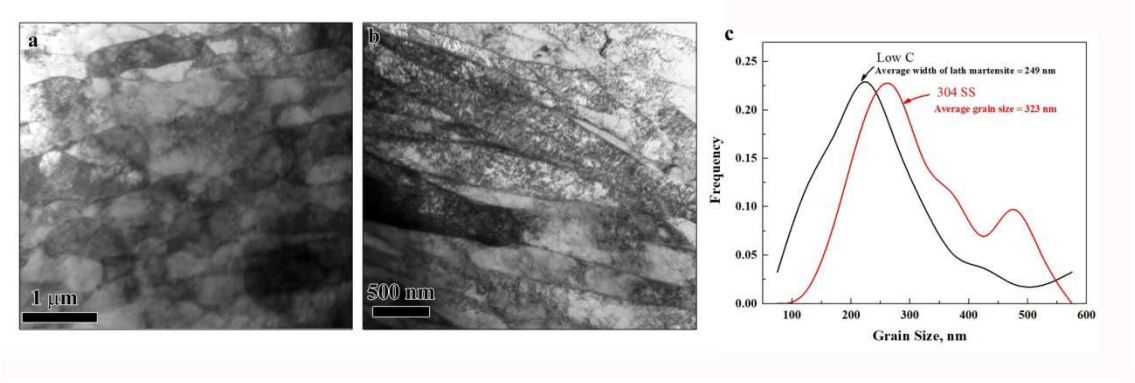

Fig. 3 TEM images near the interface in the WQ sample: (a) at the interface for the side of 304 SS; (b) with a distance of about 100 μm away to the interface for the martensite phase of low C steel. (c) The grain size distributions for both sides.

The micro-hardness distributions across the interfaces for varying samples are displayed in Fig. 4. For all samples, the micro-hardness shows a steady value away from the interfaces at both sides, as indicated in Fig. 4. The steady value of hardness for the 304 SS is similar for all samples due to the similar microstructures (as shown in Fig. 2), while the steady hardness for the low C steel shows different values for varying samples. The WQ sample has the highest steady hardness for the side of low C steel due to the formation of lath martensite, while the AN sample has the lowest steady hardness for the side of low C steel since the dislocation density is reduced in the ferrite phase after annealing. The hardness distributions across the interfaces are observed to be heterogeneous for varying samples due to the inhomogeneous microstructure near the interfaces. An interfacial zone (IZ) can be defined for varying samples, in which the hardness exhibits a heterogeneous distribution [26]. The hardness is observed to gradually decrease from the interface towards the edge of IZ at the side of 304 SS for all samples since the average grain size is smaller at the interface. For the HR and AN samples, the hardness is observed to show a slight increase from the interface towards the edge of IZ at the side of low C steel since the area at the interface has a larger grain size. While the hardness is observed to increase significantly from the interface towards the edge of IZ at the side of low C steel for the WQ sample, which has been revealed to be attributed to the decarburized process from the side of low C steel to the side of 304 SS during the thermo-mechanical processing [26]. It can be observed that the hardness shows a discontinuity at the interfaces for all samples. The hardness difference between the steady values of the 304 SS side and the low C steel side is relatively small for the HR laminate, while this difference becomes larger for the AN laminate and is largest for the WQ laminate. Thus the effect of hardness difference between the hard zone and the

soft zone on the mechanical properties and the evolution of the ASB in the laminates can be investigated by comparing the dynamic behaviors of the HR, AN and WQ samples.

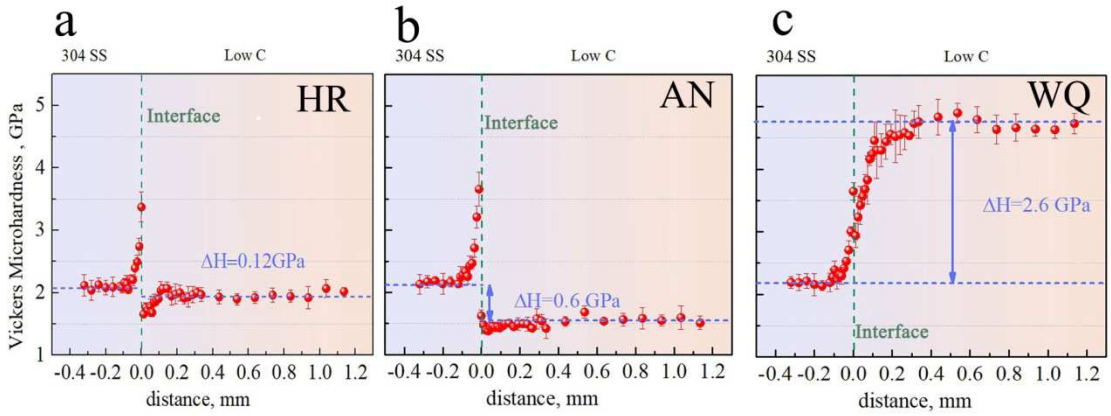

Fig. 4 The distributions of Vickers micro-hardness near the interface for varying samples: (a) HR sample; (b) AN sample; (c) WQ sample. The hardness difference for the steady values at two sides of the interface is also shown in each figure.

3.2 Dynamic shear properties

The dynamic shear properties for varying laminates are displayed in Fig. 5. Figs. 5a-5c show the dynamic shear stress-shear displacement curves for the HR, AN, WQ laminates, respectively. In these figures, the curves for the laminates are solid lines. In order to compare the dynamic shear properties of laminates with those for their homogeneous constituent plates, the dynamic shear curves for the plain constituent plates (plain 304 SS and the low C steel plates) are also displayed by dash and dotted lines in each figure. In the inset of Fig. 5c, the curves with two tests for each condition are shown, and the good repeatability can be observed. For the HR laminate, the nominal dynamic uniform shear displacement (the displacement for the maximum

dynamic shear stress) is almost the same as those for its homogeneous constituent plates, while its dynamic shear yield strength is slightly higher than that for each homogeneous constituent plate. For the AN laminate (the hard difference between the hard zone and the soft zone is larger), it is observed that both the dynamic shear yield strength and the nominal dynamic uniform shear displacement are slightly higher than those for its homogeneous constituent plates. For the WQ laminate (the hard difference between the hard zone and the soft zone is largest), the dynamic shear yield strength is the same as that of the plain low C steel plate (martensite) while the nominal dynamic uniform shear displacement is much larger than that for the plain low C steel plate with martensite phase. Then, all data points with error bars for dynamic shear yield strength vs. nominal dynamic uniform shear displacement are summarized in Fig. 5d. It is observed that the heterogeneous laminate can have superior dynamic shear properties over those for their homogeneous constituent plates.

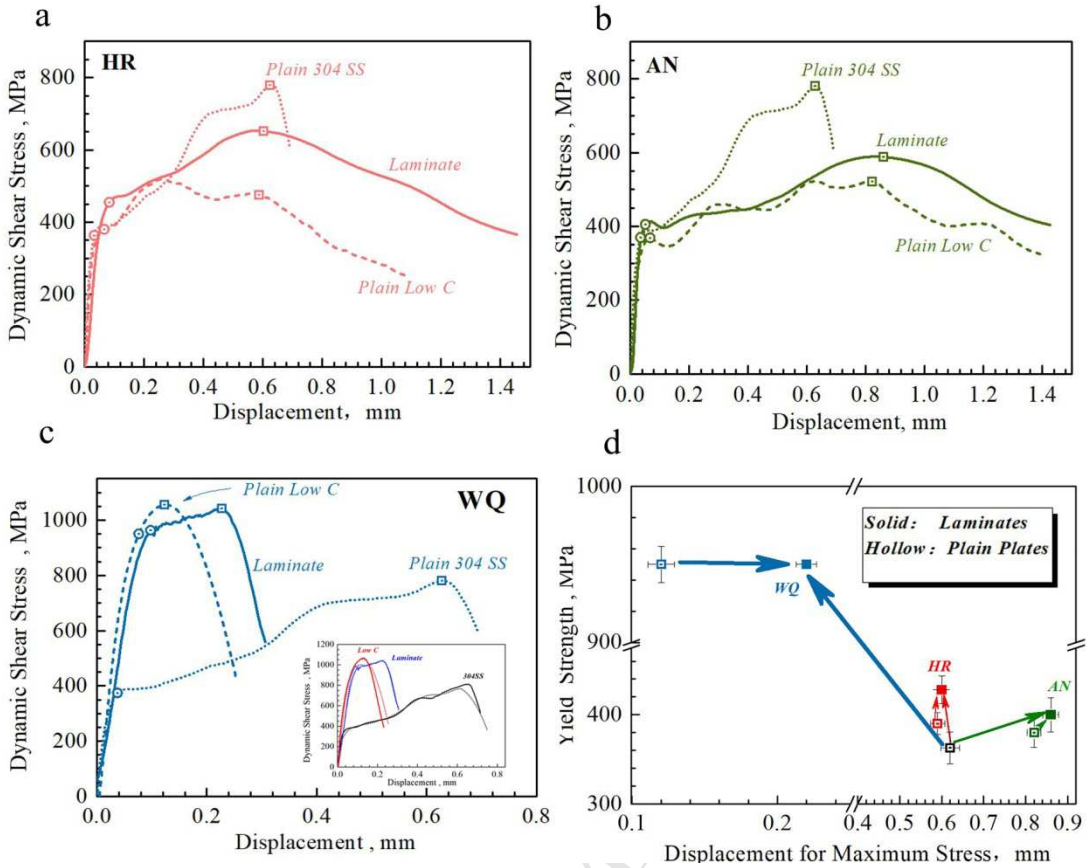

Fig. 5 Dynamic shear stress vs. shear displacement curves of varying samples: (a) HR sample; (b) AN sample; (c) WQ sample. In each figure, the curves for the plain 304 SS sample and the plain low C steel sample are also shown as dashed and dotted lines. (d) Dynamic shear yield strength vs. nominal dynamic uniform shear displacement for the data obtained in the present study (error bars are also provided).

3.3 Evolution patterns of ASB in various laminates

The propensity of strain localization for materials is generally related to the strain hardening rate and the strain rate sensitivity. For example, the flow instability under quasi-static tension is predicted fairly well by the well-known Considére criterion , and the necking starts when

$$\frac{1}{\sigma}(\frac{\partial\sigma}{\partial\varepsilon})_{\dot{\varepsilon}} \le 1 \tag{3}$$

where σ and ε are the true stress and the true strain, $\dot{\varepsilon}$ is the true strain rate.

while the flow localization under quasi-static compression is generally controlled by a material parameter α that is a function of two materials parameters [39]:

$$\alpha = (\gamma - 1)/m \tag{4}$$

where $\gamma = \frac{1}{\sigma}(\frac{\partial\sigma}{\partial\varepsilon})_{\dot{\varepsilon}}$ and m is the strain rate sensitivity.

Under dynamic loading, the susceptibility for ASB in metals and alloys is quantitatively determined by the following equation proposed by Wright [48]:

$$\chi_{ASB} = (a/m)\min\left\{1, \frac{1}{(n/m)+\sqrt{n/m}}\right\} \tag{5}$$

where n is the strain hardening exponent. While a is a non-dimensional thermal softening parameter which can be calculated by $a = (-\partial\sigma/\partial T)/\rho c$ (T is the temperature, ρ is the density, and c is the specific heat of the metal).

According to Eq. (5), materials are prone to form ASB with an increased χ_{ASB}, thus lower strain hardening ability and lower strain rate sensitivity should result in higher susceptibility for the flow instability. In general, metals and alloys with higher strength/hardness should have a lower strain hardening ability, thus ASB might nucleate in the hard zone first in the heterogeneous laminates and propagate from the hard zone to the soft zone. Here, the hard zone is defined as the area with higher strength and low strain hardening ability, while the soft zone represents the area with lower strength and higher strain hardening ability. This is checked by the nucleation and propagation patterns for various samples, shown in Fig. 6 (the cross-section along the depth). In Fig. 6d, SEM with BSE mode was used to help to characterize the microstructures since FCC austenite and BCC martensite can't be etched and revealed under OM at the same time (the close-up figures are all pictures by SEM with BSE mode).

When the specimen is totally homogeneous (plain low C steel martensite sample) or the heterogeneity is small (the hardness difference across the interface is small, e.g., the HR laminate), no shear band is observed just right before the maximum stress points and shear band through the whole sample is formed right after the maximum stress point. As indicated in the literatures, the conventional maximum stress criterion suggested that the onset of ASB should be coincident with the maximum stress point for most of homogeneous materials [38,39,44,46] although some exceptions were also observed [34]. This means that the conventional maximum stress criterion still works for the laminate with small heterogeneity and the shear band propagation speed is very fast (soon after the maximum stress point, the shear band already propagate through the whole sample). While the shear band already nucleate and propagates in the hard zone (the 304 SS side in the AN laminate, the martensite low C steel side in the WQ laminate) before the maximum stress points for the laminates with large heterogeneity, and the

shear stress does not start to drop until a larger shear displacement. The laminates can be considered as a composite of low C steel layer and 304 SS layer, thus the dynamic shear flow stress of the laminates should at least be the sum of the shear flow stress of two different layers, as calculated using the rule of mixture (ROM). When ASB is nucleated in the hard zone of the laminates, the soft zone of the laminates still has the strain hardening ability. Thus, the overall flow stress of the laminates may still increase with increasing shear displacement and start to drop at a larger shear displacement. A diffusive shear band also forms in the soft low C steel side for the AN laminate before the maximum stress point. While for the WQ laminate, no shear band is formed in the soft 304 SS side at the shear displacement of 0.30 mm (after the maximum stress point), and the propagation speed in the martensite low C steel is very slow due to the large heterogeneity across the interface. Thus, the nucleation and propagation patterns in the laminates are highly dependent on the heterogeneity across the interface. The larger hardness difference across the interface, the larger resistance for the ASB propagation, and the slower propagation speed of ASB will be. It is easy to understand that ASB may nucleate almost simultaneously in the hard and soft zones in the laminates when the hardness difference is small. While when the hardness difference is very large, ASB should be formed in the hard zone with very low strain hardening ability first and the soft zone with strong strain hardening ability should be still under homogeneous deformation. With increasing dynamic shear displacement, the formed ASB in the hard zone should propagate towards the soft zone. When the hardness difference is medium, concentrated shear band is formed in the hard zone with slightly lower strain hardening ability, while diffusive shear band is formed at the almost same time in the soft zone with slightly higher strain hardening ability.

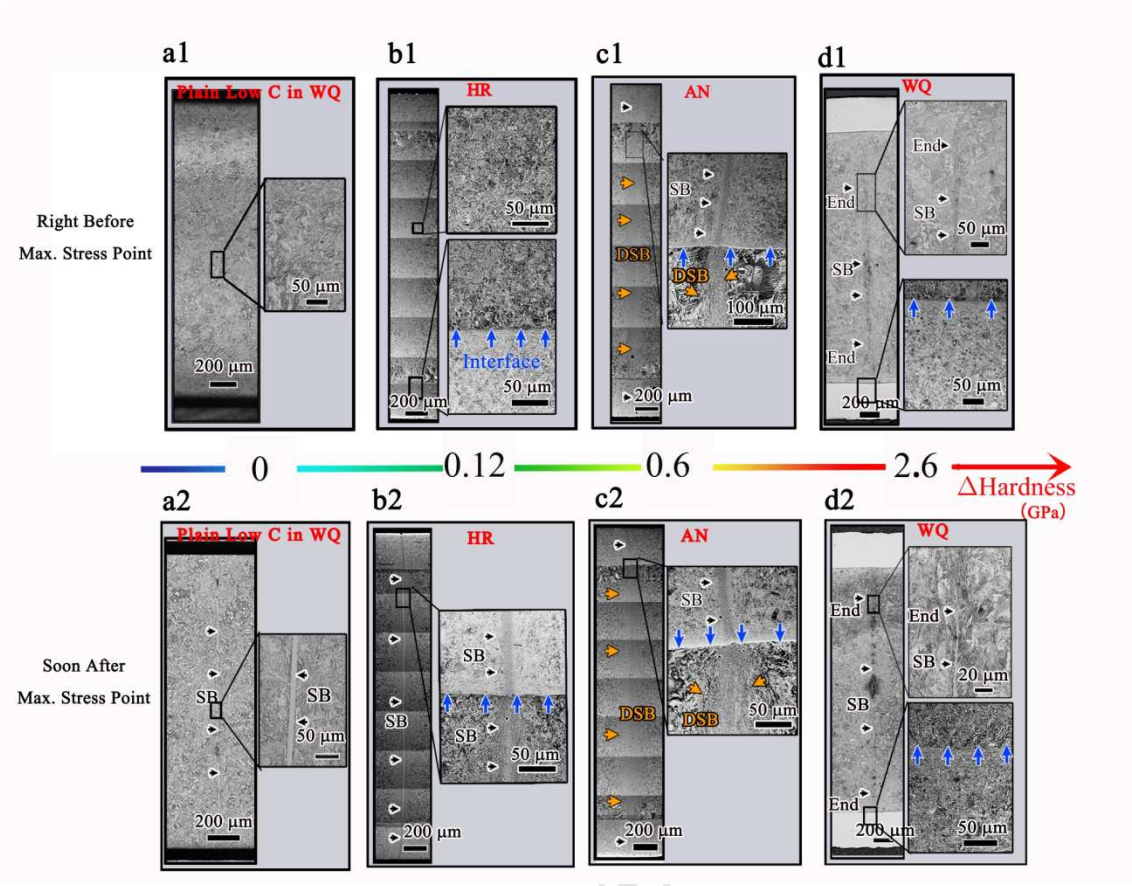

Fig. 6 Microstructrual characterizations for the cross section of varying laminates right before the maximum stress point: (a1) Plain low C steel; (b1) HR laminate; (c1) AN laminate: (d1) WQ laminate. Microstructrual characterizations for the cross section of varying laminates right after the maximum stress point: (a2) Plain low C steel; (b2) HR laminate; (c2) AN laminate: (d2) WQ laminate. It should be noted that the hardness difference for the plateau values at two sides of the interface increases in the figures from left to right. SB: shear band; DSB: diffusive shear band.

In order to reveal the shear band propagation process along the depth for the WQ sample, the images at five different displacements (0.18, 0.20, 0.25, 0.30 and 0.36 mm) are displayed in Fig. 7. Again, the close-up figures in the Fig. 7 are pictures by SEM with BSE mode since FCC austenite and BCC martensite can't be etched and

revealed under OM at the same time. The shear displacement at the maximum stress points is 0.22 mm for the WQ laminate (Fig. 5). In previous papers [49-51], it is indicated that once a shear band is nucleated in a specific location, the shear band can propagate with a fast speed (several hundred to several thousands of m/s) in homogeneous materials, which is determined by a number of material parameters and the applied shear impact velocity. The shear displacement is 0.12 mm at the maximum stress point for the plain low C steel sample (with martensite phase), which indicates that the shear band already exists in the plain low C steel sample after 0.12 mm of shear displacement (see Fig. 5c). While at the shear displacement of 0.18 mm (Fig. 7a), no shear band is observed in the whole cross-section for the WQ laminate. These observations indicate that the shear band nucleation is inhibited when the hard low C steel zone is in the laminate instead of in plain condition. A shear band is nucleated at the center of the low C steel zone (with martensite phase) and already propagates with a distance towards the interfaces at the shear displacement of 0.20 mm (at the time of about 33.6 μs after impact) in the WQ laminate (Fig. 7b). With increasing shear displacement, the shear band propagates further towards the interfaces. The shear band length increases from 1.56 mm to 2.06 mm at the shear displacement of 0.25 mm (at the time of about 40 μs after impact) and the shear band length becomes 2.36 mm at the shear displacement of 0.30 mm (at the time of about 46.4 μs after impact). Finally, at the shear displacement of 0.36 mm (at the time of about 51.6 μs after impact), the shear band propagates across the interface, and the shear band length covers the whole cross-section. Then, the average propagation velocity of the shear band along the depth in the WQ laminate can be estimated by dividing the propagating distance by the time interval, which is about 63 m/s. This propagation velocity is very similar to that for gradient structure [45] and is an order of magnitude lower than that in homogeneous metals [49-

51]. This delayed propagation of shear band can be attributed to the strain gradients and the strain partitioning between the hard zone and the soft zone [8,11,13,45].

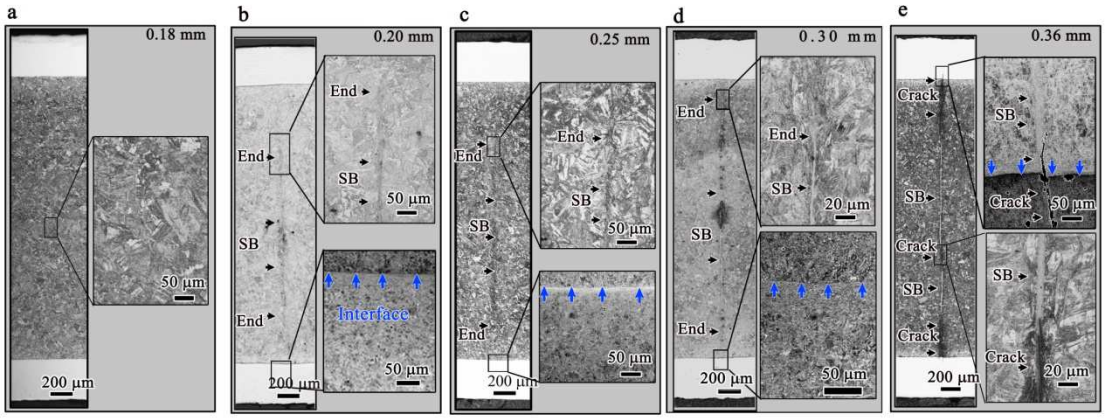

Fig. 7 Microstructrual evolution for the cross section of WQ laminate at five different interrupted shear displacements: (a) 0.18 mm, (b) 0.20 mm, (c) 0.25 mm, (d) 0.30 mm and (e) 0.36 mm.

It should also be noted that the shear band is already nucleated in the hard zone of the WQ laminate even before the maximum stress point, thus the maximum stress criterion in which the ASB should not be nucleated until the stress drop [38-40,44-46] is no longer applicable to the heterogeneous laminates. As indicated from Figs. 5 and 7, the shear band already propagates a distance in the hard zone of the WQ laminate at the shear displacement of 0.20 mm, while the shear stress does not start to drop until a larger shear displacement of 0.22 mm. These observations are very similar to those in gradient structure, and the underlying mechanisms and the corresponding discussions can be referred to the previous paper [45].

3.4 Strain hardening mechanisms of laminates under dynamic shear loading

The observed good ductility and the strong strain hardening behavior under dynamic shear loading for the WQ laminate raise a critical question: where and how is the strain hardening achieved? To resolve this issue, we measured the micro-hardness (Hv) distributions near the interface at three interrupted shear displacements (0.18, 0.20, 0.25 mm). The corresponding hardness increment (ΔHv) distributions near the interface are also shown in the Fig. 8, and ΔHv can be considered as an indicator for the magnitude of hardening retained after unloading. When the shear displacement is 0.18 mm and no shear band is formed at this moment, the 304 SS zone contributes mainly to the overall strain hardening of the laminate while the low C steel zone also has a relatively smaller contribution for the hardening behavior. When the shear displacement is increased from 0.18 mm to 0.20 mm, the 304 SS zone continues to provide strain hardening while the low C steel zone shows almost no strain hardening during this shear displacement increment. While, the zone close to the interface for the side of low C steel starts to provide extra strain hardening again when the shear band approaches the interface at the shear displacement of 0.25 mm. This strain hardening ahead the propagation tip of shear band might be attributed to the plastic deformation zone at the tip of shear band.

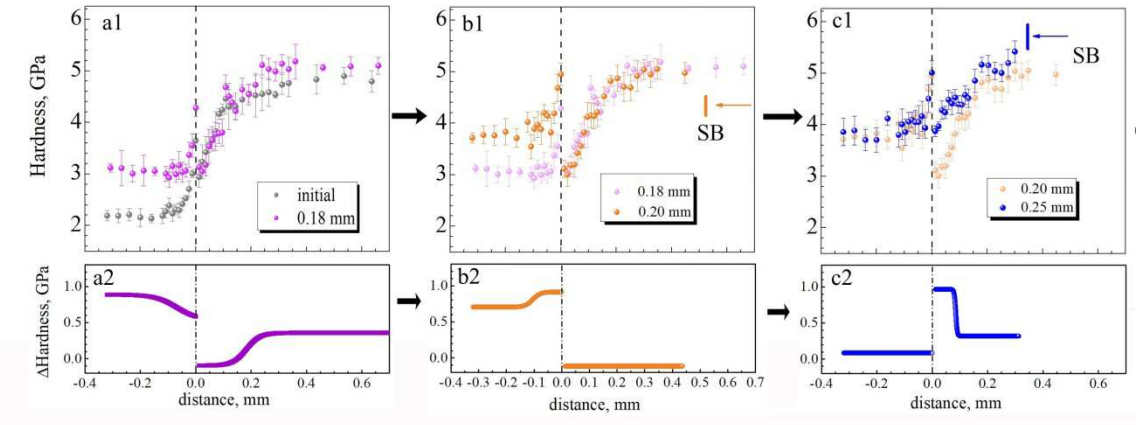

Fig. 8 Evolution of micro-hardness distributions near the interface for the WQ sample: (a1) from 0 to 0.18 mm; (b1) from 0.18 to 0.20 mm, (c1) from 0.20 to 0.25 mm. The corresponding distributions near the interface for the hardness increment are also displayed in (a2)-(c2).

In order to investigate the strain hardening and the mechanical incompatibility at the area of IZ during the dynamic shear loading, the EBSD images (IPF and phase images) and the corresponding GNDs distributions for the area of IZ (for the side of 304 SS) at various dynamic shear displacements (0, 0.20, 0.25, 0.30 mm) are characterized and provided in Fig. 9. The IPF images are shown in Figs. 9a1-9d1, while the phase images are displayed in Figs. 9a2-9d2. It can be observed from the phase maps that almost no phase transformation occurs for the side of 304 SS during the dynamic shear loading. The small amount of BCC phase at the interface might be the martensite from the side of low C steel since the interface is not perfectly straight. As mentioned in our previous paper [26], mechanical incompatibilities across interfaces occur during the tensile deformation for the laminates, resulting in strong strain gradient and high density of GNDs at the area of IZ. Under dynamic shear loading, the strain partitioning between the soft 304 SS side and the hard low C steel martensite side should also occur, resulting in high density of GNDs. While, how the density of GNDs evolves with increasing dynamic shear displacement is interesting and should be provided. In the current study, KAM method was used to obtain the density of GNDs at various dynamic shear displacements (0, 0.20, 0.25, 0.30 mm) for the area of IZ. The density of GNDs at any point can be estimated as following [52,53]:

$$\rho_{GND} = \frac{2\theta}{lb} \tag{6}$$

where, θ is the misorientation angle, l represents the unit length (100 nm in the present research), and b stands for the Burger's vector (0.253 nm for 304 SS, 0.248 nm for low C steel).

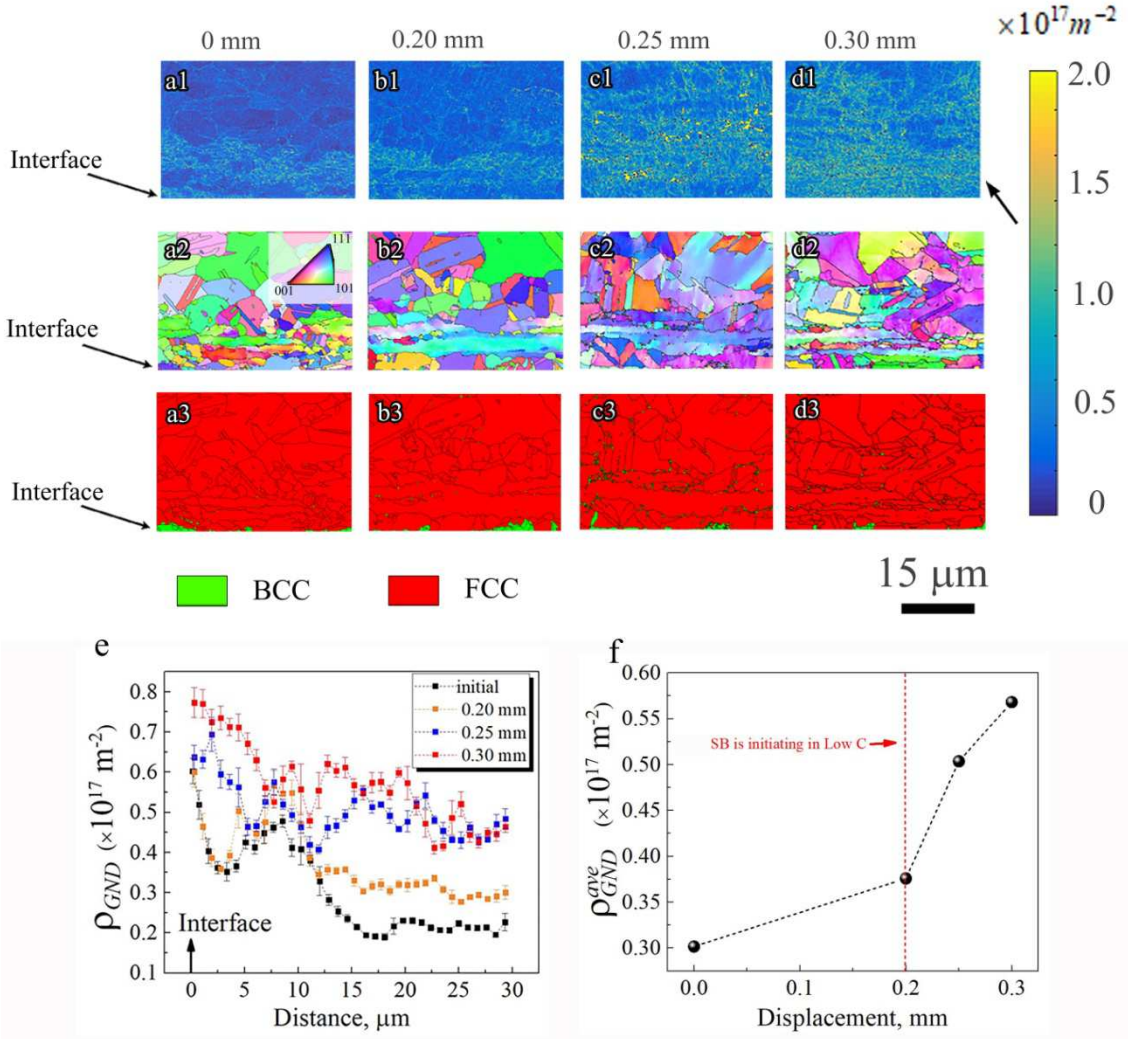

Fig. 9 Microstructure evolution at the area of IZ for the side of 304 SS at varying shear displacements (0, 0.20, 0.25, 0.30 mm) during the dynamic shear loading for the WQ laminate: (a1-d1) GND density maps; (a2-d2) IPF images; (a3-d3) phase distribution

images. (e) Distributions of GND density vs. the distance from the interface at various dynamic shear displacements (0, 0.20, 0.25, 0.30 mm) for the WQ laminate. (f) The average density of GNDs vs. the applied dynamic shear displacement.

Then, maps for the density of GNDs at the area of IZ for the side of 304 SS are shown in Figs. 9a3-9d3 (at various dynamic shear displacements of 0, 0.20, 0.25, 0.30 mm). It should be noted that the grains with different grain sizes or different crystallographic orientations should have different density of GNDs at the random GBs even the distance to the interface is the same. The average density of GNDs as a function of distance from the interface (excluding the effect of random GBs [26]) is plotted in Fig. 9e for various dynamic shear displacements (0, 0.20, 0.25, 0.30 mm). It can be observed that the density of GNDs increases when the position is closer to the interface. Since the two sides for the interface show significant difference in strength, it can be easily understood that the highest GND density should be at the interface since the maximum strain gradient should be at the interface due to the largest mechanical incompatibilities between the two sides [52,53]. It can be clearly observed that the density of GNDs at the area of IZ increases with increasing dynamic shear displacement, which can be expected from the deformation physics of heterogeneous laminates [16,17,26]. Then the average density of GNDs for the observed area is plotted as a function of applied dynamic shear displacement in Fig. 9f, and the dynamic shear displacement for the initiation of shear band is also indicated by a dash line in Fig. 9f. It is observed that the average density of GNDs for the observed area increases with increasing dynamic shear displacement, while the average density of GNDs for the observed area increases even faster after the initiation of shear band. This trend indicates that the propagation tip of shear band can induce higher strain gradients and

faster increment for the density of GNDs, resulting in extra strain hardening as observed in Fig. 8. This extra hardening should help with retarding the propagation of shear band, resulting in better dynamic ductility (the dynamic shear displacement or dynamic shear strain before the maximum stress point) for the laminates.

TEM pictures near the interface for both sides in the WQ sample after dynamic shear loading with a dynamic shear displacement of 0.25 mm (the interface is not covered by ASB at this displacement as shown in Fig. 7c, thus the interface is still under homogeneous dynamic shear deformation) are displayed in Fig. 10. Fig. 10a shows the TEM picture at the interface for the side of 304 SS, and the grain size is several hundreds of nm and deformation twins (DTs) can be clearly observed. The twin boundaries (TBs) for DTs are not coherent due to the interaction between the numerical dislocations and the TBs. TEM picture with a distance of 70 μm from the interface for the side of 304 SS is displayed in Figs. 10b and 10c, and a grain size of several μm can be found. It is clearly indicated that a higher density of DTs are formed in the larger grain size under dynamic shear loading, and the twin boundary spacing (TBS) is several tens of nm. High density of dislocations can also be found near the TBs. This higher propensity for DTs in the coarse grains has been reported before [54]. As reported in the previous research [55], three possible interactions between dislocations and TBs exist in the FCC metals, and two of them involve the formation of immobile dislocation locks for strain hardening. Thus, the strong strain hardening under dynamic shear loading at the side of 304 SS can be attributed to the formation of DTs and the dislocation behaviors near the TBs. TEM pictures with a distance of 100 μm from the interface for the side of low C steel are shown in Figs. 10d and 10e. Then the statistical distributions for the width of the lath martensite phase before and after dynamic shear loading are displayed in Fig. 10f based on numerical TEM images. The average width after

dynamic shear loading can be estimated and the width of lath martensite was found to change from 249 nm to 101 nm after dynamic shear loading. This observation indicates that the lath martensite is sheared and elongated under dynamic shear loading, and the feature size of lath martensite is refined. This grain refinement should be the origin for the strain hardening in the martensite phase under dynamic shear loading, which is very similar to the hardening in twinning-induced plasticity (TWIP) steels by DTs (so called dynamic H-P effect in TWIP steels) [56]. As we know, the flow stress/strength of smaller grains is higher than that of larger grains due to the well-know Hall-Petch relation. Thus, the flow stress of the whole sample can be elevated after grain refinement, resulting in strong strain hardening. Moreover, the strain hardening due to the grain refinement can be estimated by the grain size before deformation (d_{before}) and the grain size after deformation (d_{after}) as following: $\Delta\sigma = (K_{HP}\overline{d}_{after}^{-1/2} - K_{HP}\overline{d}_{before}^{-1/2})$, where K_{HP} is the strength coefficient for the Hall-Petch relation.

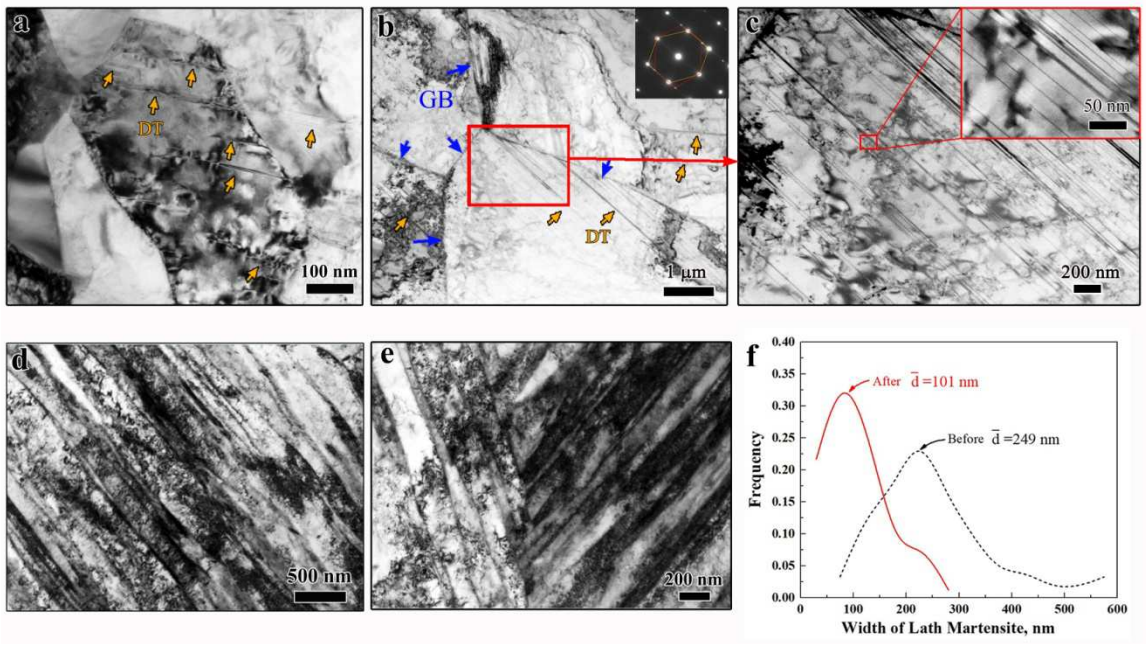

Fig. 10 TEM bright-field images near the interface for both sides in the WQ sample after dynamic shear loading (at a shear displacement of 0.25 mm). (a) TEM picture at the interface for the side of 304 SS. (b) TEM picture with a distance of 70 μm from the interface for the side of 304 SS. (c) The corresponding close-up view for the rectangular area in (c). (d) (e) TEM pictures with a distance of 100 μm from the interface for the side of low C steel. (f) The statistical distributions for the width of the lath martensite phase before and after dynamic shear loading.

It is well understood that the laminates can show better ductility and fracture resistance under tension or bending by introducing additional toughening mechanisms, such as crack deflection at the interface [57], non-localized fracture behaviors [15], inhibiting the initiation and propagation of microcracks by the well-designed residual stress [58]. Shear bands were also observed to nucleate soon after yielding at the nanostructured surface under quasi-static tensile loading in the gradient structure, while excellent tensile ductility can be achieved in the heterogeneous gradient structure by shear band delocalization in the surface nano-layer, i.e., preventing necking and delaying the propagation of shear band along the gage length [13]. In the present study, the initiation of ASB in the hard zone and propagation of ASB from the hard zone to the soft zone are inhibited in the laminates, and the extra hardening is induced at the interface and at the propagation tip of shear band, resulting in superior mechanical properties under dynamic shear loading for the laminates.

4. Conclusions

In the present study, the dynamic shear behavior of low C steel/304 stainless steel (SS) laminates have been investigated using hat-shaped specimen and interrupted technique in Hopkinson-bar experiments. The deformation mechanisms have been revealed by microstructural observations on the "frozen" samples. The main findings can be summarized as follows:

(1) Compared to the plain low C steel plate and the plain 304 SS plate, the composite laminates were observed to have better combination of shear yield strength and nominal uniform shear displacement under dynamic shear loading.

(2) ASB was observed to nucleate right after yielding (at shear displacement of 0.12 mm) in the plain martensite low C steel plate, while ASB was postponed to initiate in the martensite low C steel zone of the WQ laminate (at shear displacement of 0.20 mm). Moreover, the propagation of ASB from the hard zone to the soft zone in the WQ laminate was found be delayed, and the propagation speed was found to be one magnitude slower than that for homogeneous materials. The suppression of ASB initiation and propagation in the laminates helps for achieving better dynamic ductility.

(3) The patterns of ASB nucleation and propagation in the laminates were observed to be highly related to the hardness difference between the hard zone and the soft zone: (i) when the hardness difference is small, no shear band is observed before the maximum stress point and ASB is formed right after the maximum stress point and propagates quickly through the whole laminate; (ii) when the hardness difference is medium, concentrated shear band is formed in the hard zone and diffusive shear band is formed in the soft zone at the same time; (iii) when the hardness difference is large, ASB is formed in the hard zone first, and then propagates slowly to the soft zone.

(4) Before nucleation of ASB, the 304 SS zone contributes mainly to the overall strain hardening of the laminate while the low C steel zone also has a relatively smaller contribution for the hardening behavior. IZ was observed to provide extra hardening under dynamic shear loading by strain gradient and GNDs, which can be attributed to the mechanical incompatibility between the hard zone and the soft zone. The plastic zone at the propagation tip of shear band can also trigger extra hardening, resulting in better dynamic ductility in the laminates. The strain hardening is fulfilled by DTs in the 304 SS while by grain refinement in the martensite low C steel under dynamic shear loading. The present findings can provide insights for designing strong and tough metals and alloys for impact-tolerant applications.

Acknowledgements

The work was supported by the National Key R&D Program of China [grant number 2017YFA0204402]; the National Natural Science Foundation of China [grant numbers 11672313, 11572328 and 51601204], and the Strategic Priority Research Program of the Chinese Academy of Sciences [grant numbers XDB22040503].

Data availability

The raw/processed data required to reproduce these findings cannot be shared at this time due to technical or time limitations.

References

[1] Y.M. Wang, M.W. Chen, F.H. Zhou, E. Ma, High tensile ductility in a nanostructured metal, Nature 419 (2002) 912–915.

[2] R.Z. Valiev, R.L. Islamgaliev, I.V. Alexandrov, Bulk nanostructured materials from severe plastic deformation, Prog. Mater. Sci. 45 (2000) 103-89.

[3] K.M. Youssef, R.O. Scattergood, K.L. Murty, J.A. Horton, C.C. Koch, Ultrahigh strength and high ductility of bulk nanocrystalline copper, Appl. Phys. Lett. 87 (2005) 091904.

[4] M.A. Meyers, A. Mishra, D.J. Benson, Mechanical properties of nanocrystalline materials, Prog. Mater. Sci. 51 (2006) 427–556.

[5] L. Lu, Y.F. Shen, X.H. Chen, L.H. Qian, K. Lu, Ultrahigh strength and high electrical conductivity in copper, Science 304 (2004) 422-26.

[6] P.V. Liddicoat, X.Z. Liao, Y.H. Zhao, Y.T. Zhu, M.Y. Murashkin, E.J. Lavernia, R.Z. Valiev, S.P. Ringer, Nanostructural hierarchy increases the strength of aluminum alloys, Nature Commun. 1 (2010) 63.

[7] H.N. Kou, J. Lu, Y. Li, High-strength and high-ductility nanostructured and amorphous metallic materials, Adv. Mater. 26 (2014) 5518–5524.

[8] X.L. Wu, M.X. Yang, F.P. Yuan, G.L. Wu, Y.J. Wei, X.X. Huang, Y.T. Zhu, Heterogeneous lamella structure unites ultrafine grain strength with coarse-grain ductility, Proc. Natl. Acad. Sci. USA 112 (2015) 14501–14505.

[9] Y.H. Zhao, T. Topping, J.F. Bingert, J.J. Thornton, A.M. Dangelewicz, Y. Li, W. Liu, Y.T. Zhu, Y.Z. Zhou, E.L. Lavernia, High tensile ductility and strength in bulk nanostructured nickel, Adv. Mater. 20 (2008) 3028-3033.

[10] T.H. Fang, W.L. Li, N.R. Tao, K. Lu, Revealing extraordinary intrinsic tensile plasticity in gradient nano-grained copper, Science 331 (2011) 1587–1590.

[11] X.L. Wu, P. Jiang, L. Chen, F.P. Yuan, Y.T. Zhu, Extraordinary strain hardening by gradient structure, Proc. Natl. Acad. Sci. USA. 111 (2014) 7197–7201.

[12] Y.J. Wei, Y.Q. Li, L.C. Zhu, Y. Liu, X.Q. Lei, G. Wang, Y.X. Wu, Z.L. Mi, J.B. Liu, H.T. Wang, H.J. Gao, Evading the strength ductility trade-off dilemma in steel through gradient hierarchical nanotwins, Nat Commun. 5 (2014) 3580.

[13] F.P. Yuan, D.S. Yan, J.D. Sun, L.L. Zhou, Y.T. Zhu, X.L. Wu, Ductility by shear band delocalization in the nano-layer of gradient structure, Mater. Res. Let. 7 (2019) 12-17.

[14] R. Yuan, I.J. Beyerlein, C.Z. Zhou, Homogenization of plastic deformation in heterogeneous lamella structures, Mater. Res. Let. 5 (2017) 251-257.

[15] A.Y. Chen, D.F. Li, J.B. Zhang, H.W. Song, J. Lu, Make nanostructured metal exceptionally tough by introducing non-localized fracture behaviors, Scr. Mater. 59 (2008) 579-582.

[16] X.L. Ma, C.X. Huang, W.Z. Xu, H. Zhou, X.L. Wu, Y.T. Zhu, Strain hardening and ductility in a coarse-grain/nanostructure laminate material, Scripta Mater. 103 (2015) 57-60.

[17] X.L. Ma, C.X. Huang, J. Moering, M. Ruppert, H.W. Höppel, M. Göken, J. Narayan, Y.T. Zhu, Mechanical properties of copper/bronze laminates: Role of interfaces, Acta Mater. 116 (2016) 43-52.

[18] H. Wu, G.H. Fan, M. Huang, L. Geng, X.P. Cui, H.L. Xie, Deformation behavior of brittle/ductile multilayered composites under interface constraint effect, Inter. J. Plast. 89 (2017) 96-109.

[19] M. Ojima, J. Inoue, S. Nambu, P. Xu, K. Akita, H. Suzuki, T. Koseki, Stress partitioning behavior of multilayered steels during tensile deformation measured by in situ neutron diffraction, Scripta Mater. 66 (2012) 139-142.

[20] H.S. Liu, B. Zhang, G.P. Zhang, Delaying premature local necking of high-strength Cu: a potential way to enhance plasticity, Scripta Mater. 64 (2011) 13-16.

[21] H. Wu, B.C. Jin, L. Geng, G.H. Fan, X.P. Cui, M. Huang, R.M. Hicks, S. Nutt, Ductile-phase toughening in TiBw/Ti-Ti3Al metallic-intermetallic laminate composites, Metall. Mater. Trans. A 46A (2015) 3803-3807.

[22] S. Zheng, I.J. Beyerlein, J.S. Carpenter, K. Kang, J. Wang, W. Han, N.A. Mara, high-strength and thermally stable bulk nanolayered composites due to twin induced interfaces, Nature Commun. 4 (2013) 1696.

[23] I.J. Beyerlein, J.R. Mayeur, S. Zheng, N.A. Mara, J. Wang, A. Misra, Emergence of stable interfaces under extreme plastic deformation, Proc. Natl. Acad. Sci. 111 (2014) 4386-4390.

[24] A. Misra, J.P. Hirth, R.G. Hoagland, Length-scale-dependent deformation mechanisms in incoherent metallic multilayered composites, Acta Mater. 53 (2005) 4817-4824.

[25] C.X. Huang, Y.F. Wang, X.L. Ma, S. Yin, H.W. Höppel, M. Göken, X.L. Wu, H.J. Gao, Y.T. Zhu, Interface affected zone for optimal strength and ductility in

heterogeneous laminate, Mater. Today 21 (2018) 713-719.

[26] J.Y. He, Y. Ma, D.S. Yan, S.H. Jiao, F.P. Yuan, X.L. Wu, Improving ductility by increasing fraction of interfacial zone in low C steel/304 SS laminates. Mater. Sci. Eng. A 726 (2018) 288-297.

[27] M.X. Yang, Y. Pan, F.P. Yuan, Y.T. Zhu, X.L. Wu, Back stress strengthening and strain hardening in gradient structure, Mater. Res. Lett. 4 (2016) 141–151.

[28] X.L. Wu, Y.T. Zhu, Heterogeneous materials: a new class of materials with unprecedented mechanical properties, Mater. Res. Lett. **5** (2017) 527-532.

[29] E. Ma, T. Zhu, Towards strength-ductility synergy through the design of heterogeneous nanostructures in metals, Mater. Today **20** (2017) 323-331.

[30] M.A. Meyers, Dynamic Behavior of Materials, Wiley-Interscience, New York, USA (1994) 323-326.

[31] J.X. Xing, F.P. Yuan, X.L. Wu, Enhanced quasi-static and dynamic shear properties by heterogeneous gradient and lamella structures in 301 stainless steels, Mater. Sci. Eng. A 680 (2017) 305-316.

[32] Z.J. Xu, X.Y. Ding, W.Q. Zhang, F.L. Huang, A novel method in dynamic shear testing of bulk materials using the traditional SHPB technique, Int. J. Impact Eng. 101 (2017) 90-104.

[33] T. Suo, Y.L. Li, F. Zhao, X.L. Fan, W.G. Guo, Compressive behavior and rate-controlling mechanisms of ultrafine grained copper over wide temperature and strain rate ranges, Mech. Mater. 61 (2013) 1-10.

[34] Y.Z. Guo, Q.C. Ruan, S.X. Zhu, Q. Wei, H.S. Chen, J.N. Lu, B. Hu, X.H. Wu, Y.L. Li, D.N. Fang, Temperature rise associated with adiabatic shear band: Causality clarified, Phys. Rev. Lett. 122 (2019) 015503.

[35] C. Zener, J.H. Hollomon, Effect of strain rate upon plastic flow of steel, J. Appl. Phys. 15 (1944) 22-32.

[36] S. Nemat-Nasser, W.G. Guo, Thermomechanical response of DH-36 structural steel over a wide range of strain rate and temperatuers, Mech. Mater. 35 (2003) 1023-1047.

[37] Q. Wei, Strain rate effects in the ultrafine grain and nanocrystalline regimes influence on some constitutive responses, J Mater. Sci. 42 (2007) 1709-1727.

[38] A. Mishra, M. Martin, N.N. Thadhani, B.K. Kad, E.A. Kenik, M.A. Meyers, High-strain rate response of ultra-fine-grained copper, Acta. Mater. 56 (2008) 2770-

2783.

[39] Q. Wei, L. Kecskes, T. Jiao, K.T. Hartwig, K.T. Ramesh, E. Ma, Adiabatic shear banding in ultrafine-grained Fe processed by severe plastic deformation, Acta Mater. 52 (2004) 1859-1869.

[40] M.A. Meyers, G. Subhash, B.K. Kad, L. Prasad, Evolution of microstructure and shear-band formation in α-hcp titanium, Mech. Mater. 17 (1994) 175-193.

[41] L.J. Xiao, W.D. Song, Additively-manufactured functionally graded Ti-6Al-4V lattice structures with high strength under static and dynamic loading: Experiments, Int. J. Impact Eng. 111 (2018) 255-72.

[42] T.F. Zhou, J.J. Wu, J.T. Che, Y. Wang, X.B. Wang, Dynamic shear characteristics of titanium alloy Ti-6Al-4V at large strain rates by the split-Hopkinson pressure bar test, Int. J. Impact Eng. 109 (2017) 167-77.

[43] Y. Yang, F. Jiang, B.M. Zhou, X.M. Li, H.G. Zheng, Q.M. Zhang, Influence of shock prestraining on the formation of shear localization in 304 stainless steel, Mater. Sci. Eng. A 528 (2011) 2787-2794.

[44] F.P. Yuan, P. Jiang, X.L. Wu, Annealing effect on the evolution of adiabatic shear band under dynamic shear loading in ultra-fine-grained iron, International Journal of Impact Engineering 50 (2012) 1-8.

[45] X.D. Bian, F.P. Yuan, Y.T. Zhu, X.L. Wu, Gradient structure produces superior dynamic shear properties, Mater. Res. Lett. 5(7) (2017) 501-507.

[46] Y. Ma, F.P. Yuan, M.X. Yang, P. Jiang, E. Ma, X.L. Wu, Dynamic shear deformation of a CrCoNi medium-entropy alloy with heterogeneous grain structures, Acta Mater. 148 (2018) 407-418.

[47] M. Calcagnotto, D. Ponge, E. Demir, D. Raabe, Orientation gradients and geometrically necessary dislocations in ultrafine grained dual-phase steels studied by 2D and 3D EBSD, Mater. Sci. Eng. A 527 (2010) 2738-2746.

[48] T.W. Wright, Shear band susceptibility - work-hardening materials, Inter. J. Plast. 8 (1992) 583-602.

[49] P.R. Guduru, A.J. Rosakis, G. Ravichandran, Dynamic shear bands: an investigation using high speed optical and infrared diagnostics, Mech. Mater. 33 (2001) 371-402.

[50] A.S. Bonnet-Lebouvier, A. Molinari, P. Lipinski, Analysis of the dynamic propagation of adiabatic shear bands, Int. J. Solids Struct. 39 (2002) 4249-4269.

[51] Q. Xue, M.A. Meyers, Self-organization of shear bands in titanium and Ti-6Al-4V alloy, Acta Mater. 50 (2002) 575-596.

[52] H. Gao, Y. Huang, W.D. Nix, J.W. Hutchinson, Mechanism-based strain gradient plasticity – I. Theory, J. Mech. Phys. Solids 47 (1999) 1239–1263.

[53] L.P. Kubin, A. Mortensen, Geometrically necessary dislocations and strain gradient plasticity: a few critical issues, Scr. Mater. 48 (2003) 119–125.

[54] X.L. Wu, Y.T. Zhu, Inverse grain-size effect on twinning in nanocrystalline Ni, Phys. Rev. Lett. 101 (2008) 025503.

[55] L. Lu, Z.S. You, K. Lu, Working hardening of polycrystalline Cu with nanoscale twin, Scr. Mater. 66 (2012) 837-842.

[56] M. Madivala, A. Schwedt, S.L. Wong, F. Roters, U. Prahl, W. Bleck, Temperature dependent strain hardening and fracture behavior of TWIP steel, Int. J. Plast. 104 (2018) 80-103.

[57] D.R. Bloyer, K.T.V. Rao, R.O. Ritchie, Fracture toughness and R-curve behavior of laminated brittle-matrix composites, Metall. Mater. Trans. A 29A (1998) 2483-2496.

[58] D.J. Green, R. Tandon, V.M. Sglavo, Crack arrest and multiple cracking in class through the use of designed residual stress profiles, Science 283 (1999) 1295-1297.